Electrodeposited Structurally Stable V_2O_5 Inverse Opal Networks as High Performance Thin Film Lithium Batteries

*Eileen Armstrong[a,†], David McNulty[a], Hugh Geaney[a] and Colm O'Dwyer[a,b]**

[a] Department of Chemistry, University College Cork, Cork, T12 YN60, Ireland
[†] Present address: Department of Life Science, Institute of Technology, Sligo, F91 YW50, Ireland
[b] Micro-Nano Systems Centre, Tyndall National Institute, Lee Maltings, Cork, T12 R5CP, Ireland

Keywords: Inverse Opal, Vanadium Oxide, Lithium Batteries, Cathode, Energy Storage

Abstract

High performance thin film lithium batteries using structurally stable electrodeposited V_2O_5 inverse opal (IO) networks as cathodes provide high capacity and outstanding cycling capability and also demonstrated on transparent conducting oxide current collectors. The superior electrochemical performance of the inverse opal structures were evaluated through galvanostatic and potentiodynamic cycling and the IO thin film battery offers increased capacity retention compared to micron-scale bulk particles from improved mechanical stability and electrical contact to stainless steel or transparent conducting current collectors from bottom-up electrodeposition growth. Li^+ is inserted in to both structures at different potentials, and correlated to a preferential exposure of insertion sites of the IO network to the electrolyte. Additionally, potentiodynamic testing quantified the portion of the capacity is stored as surface bound capacitive charge. Raman scattering and XRD characterization showed how the IO allow swelling into the pore volume rather than away from the current collector. V_2O_5 IO coin cells offer high initial capacities, but capacity fading can occur with limited electrolyte. Finally, we demonstrate that a V_2O_5 IO thin film battery prepared on a transparent conducting current collector with excess electrolyte exhibits high capacities (~200 mAh g^{-1}) and outstanding capacity retention and rate capability.

Introduction

With the rapid and ever increasing growth in portable electronics and the growing need for safer and longer range electric and hybrid powered vehicles, the demand for light weight, high performance batteries with high power and energy densities, has never been more prevalent. The active material electrodes currently used in most Li-ion batteries often suffer performance issues due in some part to the disordered and brittle nature of these materials. For this reason, a substantial amount of research is currently underway to find materials and material architectures for batteries and supercapacitors that can deliver the desired improvements in battery performance without exacerbating side reactions to maintain safety and chemical stability for long service life, and to improve cathode capacity. [1-9] Recently, three dimensional macroporous or mesoporous (3DOM) architectures, in particular inverse opal (IO) architectures, [10-12] have shown a lot of potential for providing a large active surface area within a continuously-interconnected electrode structure. [13-19]

Lithium cobalt oxide ($LiCoO_2$) is currently the most commonly used cathode material in commercial Li-ion batteries. However, its increasing scarcity, high cost and poor cycle life has led to a growing interest into finding a replacement Co-free cathode material that is low in cost and can provide high specific capacity values while withstanding high charge/discharge rates. One such material receiving a lot of attention as a replacement cathode material, due to its low cost, availability and high energy density, is vanadium pentoxide (V_2O_5) [20-22]. Vanadium pentoxide (V_2O_5) has a particularly attractive mixed valence, V^{4+} and V^{5+}, making it an ideal candidate for a large number of redox-dependent applications. [23-24] For this reason, the development [25-29] and synthesis of three-dimensional [10, 30], nanostructured, porous V_2O_5 materials that can provide the desired surface area while accommodating foreign species with limited structural deformation during battery operation is tremendously important. [31] Recent nano-networks have shown promise in improving rate capability in this material. [32]

We have previously reported efficient methods for controlling 2D and 3D vanadium oxide inverse opal structures and hollow sphere arrays with a vanadium oxide solution. [33-34] Engineered nanoscale materials that have 3D ordered porosity can in principle accommodate electrolyte within the material and provide shorter diffusion pathways for efficient lithiation of the active material. [11, 14, 35] A key challenge that is a basis for the use of ordered material approaches, is the problem of limited ionic and electronic transport kinetics in standard battery materials that do not have as-deposited sub-structure that allow electrolyte infiltration, or from thicker materials that have solid state diffusion limitations. These become important especially if higher charge rates are required without runaway of the charge overpotential to maintain coulometric efficiency. [3-5, 11, 18, 35-37] Engineering electrode material structure, phase and chemical potential from the atomic scale to the electrode scale is important for enhancing stable capacity retention at high rates.

For materials that in nature, define the colours of many insects, marine life and bird feathers,[38-41] i.e. photonic crystals, electrochemical modification via Li insertion and removal at different rates can alter the crystal structure and periodicity from volumetric swelling causing a variation in the index contrast that is related to changes in the structural, electronic, and (electro)chemical nature of the battery electrode. Diagnostic examining of thin film battery materials that benefit from porosity is best achieve on transparent substrates, and so here we demonstrate exceptional performance of IO materials on F-doped tin oxide current collectors as a semi-transparent thin film lithium battery.

In this work, the electrochemical performance of a V_2O_5 inverse opal (IO) is evaluated and compared to bulk V_2O_5 and electrodeposited non-IO samples. The electrochemical performance of each sample is compared through galvanostatic cycling and cyclic voltammetry. By quantitative analysis of the relative contributions to the total stored change, we prove that IO cathodes maintain a dominant intercalation-mode response, even at higher

scan rates. Finally the electrochemical performance of a semi-transparent V_2O_5 IO thin film lithium battery is demonstrated.

Experimental section

Opal template and V_2O_5 IO cathode electrodeposition

Colloidal crystal templates were formed on ~1 cm × 1 cm of conductive substrates of stainless steel (SS) foil, ITO/FTO coated glass of ~ 2 cm × 1 cm total area by the electrophoretic deposition of 350 nm diameter polystyrene (PS) spheres at a constant potential of 2.0 V. The PS sphere solutions were prepared using 0.8 mL of the 2.5 wt% sulfated PS solution mixed with 4.3 mL ethanol, and ~ 80 μL of 30% aqueous NH_4OH to ensure a pH between 8 and 10. This produced a final concentration of spheres of ~0.4%. Electrophoretic deposition produced multilayer colloidal crystal opal PS templates with the hexagonal (111) plane grown parallel to the substrate surface. Templates were then gently annealed for ~2 h at 70°C to promote adhesion and structural stability for electrodeposition.

Vanadium pentoxide was infilled by electrodeposition at room temperature using a VersaSTAT3 Potentiostat. A constant potential of 2.0 V was applied versus a saturated calomel (SCE) reference electrode in a three-electrode cell with a platinum mesh as counter electrode and the PS template-coated substrate as the working electrode. The electrolyte consisted of a 0.25 M $VOSO_4.\chi H_2O$ solution in 1:1 (v/v) mixture of deionized water and ethanol. The final solution was made by adding 2.53 g of $VOSO_4.\chi H_2O$, used as purchased from Sigma Aldrich, to a mixture of 20 ml of deionized water and 20 ml of ethanol. The addition of ethanol to the solution reduces the surface tension between electrolyte and the PS template, increasing infiltration of the electrolyte to substrate surface. [42-43] After deposition, samples were heated to 300°C for 24 h to remove the spheres, resulting in the formation of a

network of crystalline V_2O_5. The electrodeposition of vanadium oxide was performed for PS templates on ITO-coated glass, FTO-coated glass and SS foil substrates. For comparison, vanadium oxide was also electrodeposited under similar conditions on to substrates without PS templates in place. These planar deposits were also heated at 300°C for 24 h to ensure the formation of crystalline V_2O_5. The mass of stainless steel changes slightly on heating due to oxide formation, and so all SS substrates were therefore pre-heated to 300°C and allowed to cool before sphere deposition to improve the accuracy of the mass calculation. Limited thermal oxide growth (blueing) on SS post-deposition was not found to influence the adhesion of the planar nor IO structures that were electrodeposited.

Structural and Electrochemical Characterization

SEM analysis was performed using an FEI Quanta 650 FEG high resolution SEM at an accelerating voltage of 10 kV. XRD analysis was performed using a Phillips Xpert PW3719 diffractometer using Cu Kα radiation. (Cu Kα, $\lambda = 0.15418$ nm, operation voltage 40 kV, current 40 mA). All electrochemical results presented in this report were performed using a BioLogic VSP Potentiostat/Galvanostat. The electrolyte consisted of a 1 mol dm^{-3} solution of lithium hexafluorophosphate salts in a 1:1 (v/v) mixture of ethylene carbonate in dimethyl carbonate + 3 wt% vinylene carbonate. The electrochemical properties of V_2O_5 were investigated in a half cell configuration against a pure Li counter electrode in a two electrode, stainless steel split cell. No additional conductive additives or binders were added. The mass loading of the active materials was ~ 1-2 mg/cm^2. Cyclic voltammetry with was performed using various scan rates in a potential window of 4.0 – 1.2 V. Galvanostatic and rate capability testing was performed using a range of different C-rates, where 1C = 147 mAh g^{-1} (at $\chi \sim 1$ in $Li\chi V_2O_5$), in a potential window of 4.0 – 1.2 V. Galvanostatic cycling was also performed in 3-electrode flooded cell, consisting of a glass vial and Teflon lid. The reference and counter electrodes in 3-electrode tests were both Li foil.

Results and Discussion

SEM images of vanadium oxide electrode materials prepared without (Edep) and with the PS opal template are presented in Fig. 1(a) and (b), respectively. The electrodeposited samples without the template possess an undulating film-like structure, without any obvious ordering (Fig. 1(a)). Annealing of the infilled opal template resulted in a vanadium oxide inverse opal (IO) structure (Edep IO), seen in Fig. 1(b). The conditions were chosen to ensure the IO periodic pore volume and diameter matched the parent opal template (~350 nm spheres in this case). The porous nature of the IO makes in an ideal structure for a battery electrode material as a greater surface area of the active material will likely be in direct contact with the electrolyte. The ordered porosity forms in domains separated by cracks, allowing efficient volumetric infiltration by the electrolyte from the IO surface down to the current collector electrode. Growth by electrodeposition rather than other infilling methods ensures that any IO formation is due to electrochemical reduction processes that rely on consistent electrical connection to the underlying current collector. TEM images of an Edep IO sample are shown in Fig. S1. Figure S1(c) shows that the walls of the IO structure are comprised of agglomeration of nanoscale crystallites. The crystalline structure of the walls of the IO are indicated by the layers of vanadium oxide which can be seen in Fig. S1(d). The interlayer spacing measured from TEM images was ~ 0.436 nm, which corresponds to the (001) interplanar spacing for orthorhombic V_2O_5.

XRD patterns for Edep and Edep IO in Fig. 1(c) and (d), respectively confirms crystalline orthorhombic V_2O_5 (JCPDS 00-041-1426) with a *Pmmn* space group for both Edep and Edep IO materials. We previously showed that the tortuosity of the opal template free-volume does not impeded the mechanism of electrodeposition, and a progressive, complete infilling does efficiently occur [33]. In fact, the measured current during potentiostatic growth scales as a function of the free area of the current collector, maintaining high quality electrical contact at all time. By comparison of the diffraction reflections, the Edep IO structure

maintains remarkable similarity to the planar deposit phase of vdW layered V_2O_5, which is ideal for cation intercalation. [21, 44] Notably, higher index reflections are relatively more intense compared to the (001) reflection in IO since the closed bilayered V_2O_5 slab layered structure is arranged perpendicular to the open-topped structure [45], rather than across the surface for the Edep non-templated deposit – the majority of access points facilitate cation insertion into the side of the layered vanadate crystals unlike the planar deposit which predominantly maintain a (001) surface in contact with electrolyte. This ensures more efficient cation insertion. The (001) reflection has a much higher relative intensity in planar electrodeposits compared to IOs because the V_2O_5 (001) planes of the layered orthorhombic materials form predominantly parallel to the substrate. The IO by comparison, crystallizes with (001) planes, and the (*hk*0) and (*h*0*l*) reflections oriented in 3D, with less preferential texture.

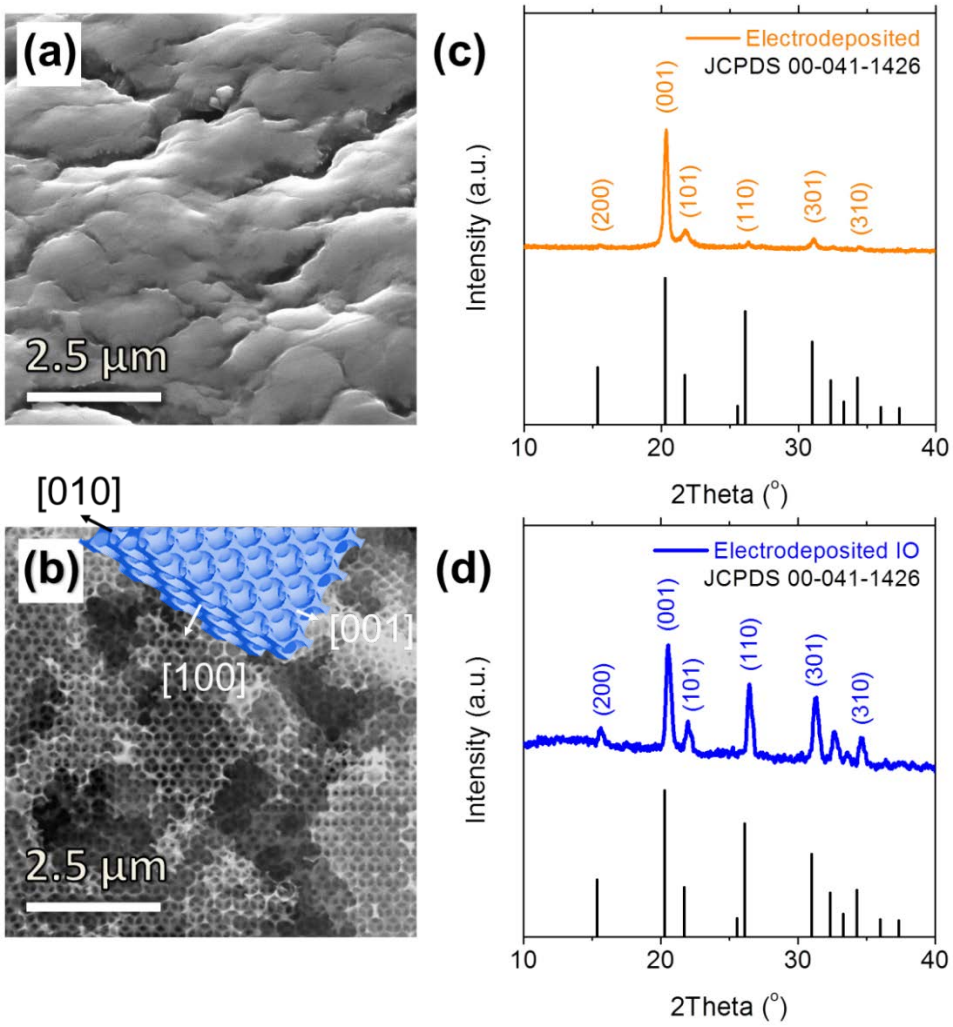

Fig. 1. SEM images of (a) electrodeposited V_2O_5 and (b) electrodeposited V_2O_5 IO on SS current collectors. Corresponding XRD patterns of (c) electrodeposited and (d) electrodeposited IO V_2O_5 compared to the JCPDS standard for orthorhombic layered V_2O_5. The inset indicate relative orientation of the (001) and (010) planes in the IO structure, compared to a dominant (001) closed crystalline slab for planar V_2O_5. HRETM analysis of the IO is provided in Fig. S1.

The cyclic voltammetric characterization of the Edep and Edep IO samples is presented in Fig. 2. Edep and Edep IO samples were galvanostatically cycled for 10 cycles using a C-rate of 0.2 C, shown in Fig. 2. Samples prepared with micron-scale, orthorhombic V_2O_5 (Bulk V_2O_5), were also galvanostatically tested under the same conditions. The voltage profiles of the first cycle and the differential capacity plots for the Edep, Edep IO and bulk V_2O_5 samples are shown in Fig. S2. The initial discharge curves for all samples demonstrated the different contributions to initial capacity from the ternary $Li_\chi V_2O_5$ phases. [46] The lower

potential limit for all galvanostatic tests was 1.2 V, discharging orthorhombic V_2O_5 to this potential is known to cause an irreversible reaction which leads to the formation of an ω-$Li_\chi V_2O_5$ phase. The electrochemical performance of ω-$Li_\chi V_2O_5$ has been reported to be quite stable in terms of capacity retention during cycling. [47] While a greater initial capacity is linked to the $Li_\chi V_2O_5$ phase ($0 < \chi < 1$) for the bulk material in Fig. 2(c), capacity retention is superior for IO structures, which reach this phase with a lesser specific capacity on the 1st cycle. The discharge and charge voltage profiles of the 2nd, 5th and 10th cycles for the Edep and Edep IO cathodes are shown in Fig. 2(a) and (b) respectively. It can be seen that after the first cycle the discharge and charge curves for the Edep and Edep IO cathodes are quite smooth, without any discrete voltage plateau. Similar smooth curves have been observed for V_2O_5 IO vs Li/Li^+ and also with other nanostructured vanadium oxide electrodes [20-21, 48]. The specific capacity of the Edep sample after the second discharge was ~ 138.5 mAh g^{-1} corresponding to a Li mole fraction of $\chi \sim 0.94$), which is marginally higher than the Edep IO capacity estimated to be ~ 112.4 mAh g^{-1} (at $\chi \sim 0.76$ in $Li\chi V_2O_5$). The phase transitions seen in the discharge curves of both samples correspond to the ε-$Li_\chi V_2O_5$ phase (typically $0.35 < \chi < 0.7$) and the δ-phase ($0.9 < \chi < 1.0$). The quantity of intercalated lithium is noted to increase slightly from the 2nd to 10th cycle for both Edep and Edep IO with cycling.

A comparison of the discharge capacities for bulk V_2O_5, Edep and Edep IO samples over the first 10 cycles is shown in Fig. 2(c). The initial capacity was highest for the bulk V_2O_5, which suffered the most significant capacity fade and consequently had the lowest capacity values after 10 cycles – the IO materials exhibits the least 1st cycle capacity fade. The specific capacity values for the Edep and Edep IO cathodes increased over the first 10 cycles. After the 1st cycle however, the Edep and Edep IO structures, without conductive additives or binders, were electrodeposited directly on the current collector and maintain good electrical contact. As can be seen in Fig. 1(a) and (c) the Edep sample is comparable to a thin film of orthorhombic V_2O_5, this film may be in better electrical contact with the stainless steel current

collector than the porous IO structure.

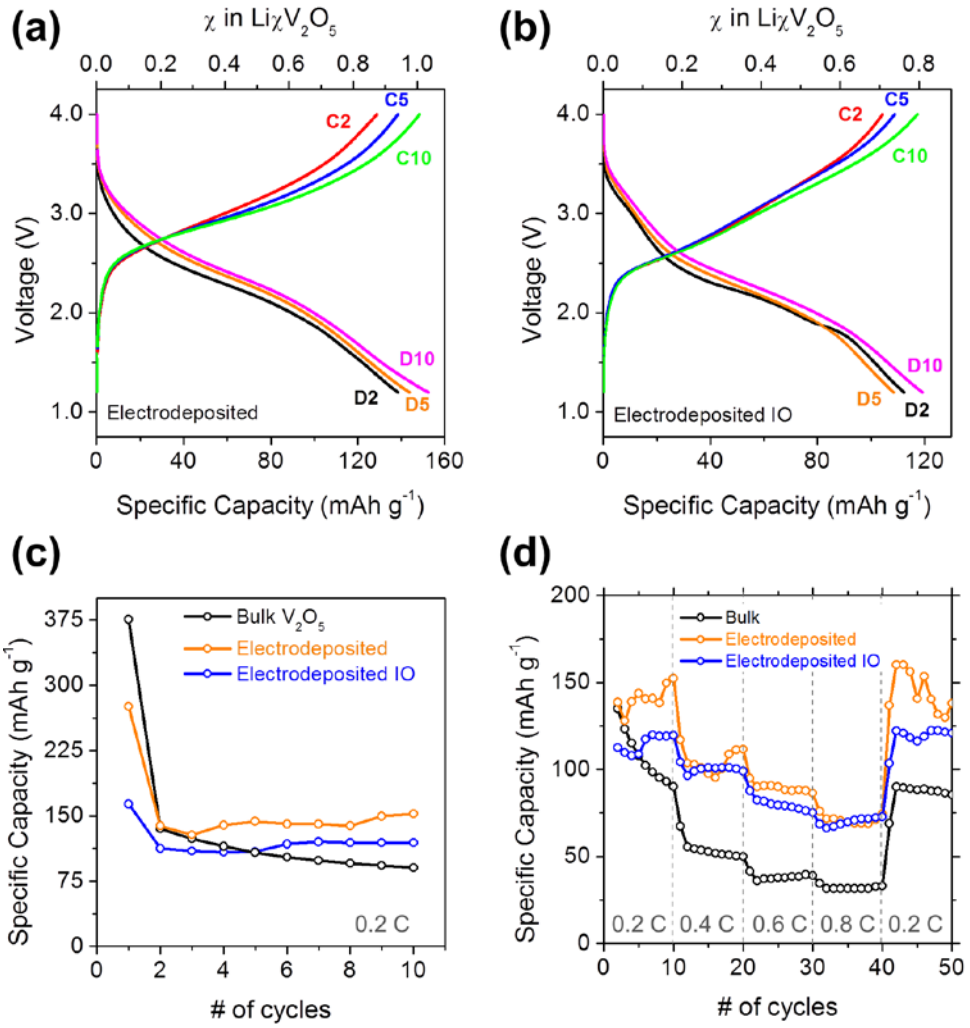

Fig. 2 Discharge and charge voltage profiles for (a) electrodeposited (Edep) and (b) electrodeposited IO (Edep IO), at a C-rate of 0.2 C. (c) Specific capacity comparison over the first 10 cycles and (d) rate capability test for Edep, Edep IO and bulk V_2O_5 powder lithium battery cathodes over 50 cycles, using C-rates ranging from 0.2 C- 0.8 C.

In order to investigate the rate capability of the electrodeposited V_2O_5 samples they were cycled at various C-rates ranging from 0.2 C- 0.8 C, as shown in Fig. 2(d). Both the Edep and Edep IO samples performed better than bulk V_2O_5, in terms of capacity retention and recovery. With respect to the Edep IO material (blue), an increase in C-rate from 0.2 C to 0.4 C after the 10^{th} cycle caused a decrease in specific capacity from ~104.4 mAh g^{-1} to ~96.4 mAh g^{-1}. For a C-rate of 0.6 C, the specific capacity decreased to a value of 82.1 mAh g^{-1} and a further increase in C-rate to 0.8 C resulted in a decrease in specific capacity to ~65.6 mAh g-

[1]. However, when the C-rate was returned to its initial value of 0.2 C the specific capacity recovered to ~121.90 mAh g^{-1}. This recovery in specific capacity indicates a high degree of stability for the electrodeposited V_2O_5 IO as a cathode material. [49] The Edep material (yellow) demonstrated a similar recovery in specific capacity values on return to the initial current after the 40th cycle. From Fig. 2(d), it is clear that both the Edep and Edep IO samples demonstrate significant rate capability with capacity values recovering to initial values, in the final segment as the applied current was returned to its initial value. It is also clear that both samples exhibit far superior electrochemical performance compared to bulk V_2O_5 – the Edep IO exhibits the most stable capacity retention during cycling and all rates, with the least initial capacity fading during cycling at each rate and the least percentage reduction in capacity at higher rates (which improves with electrolyte flooded IO materials, detailed further on).

The cyclic voltammetric response of the Edep and Edep IO samples at slow scan rates of 0.1 mV s^{-1} in a potential range of 4.0 – 1.2 V for 10 cycles is shown in Fig. 3. The profile of the CV curves is highly indicative of the phase and structural transitions within the material due to lithium insertion and removal. [50] There is a marked contrast in the first cycle for the Edep and Edep IO samples as can be seen in Fig. 3(a) and (b), respectively. The measured current of the negative scan for the Edep sample decreased gradually from 4.0 to 2.5 V. The main Li insertion peak occurred at ~ 2.08 V and there was a less significant insertion peak at ~ 1.67 V. A series of discrete Li^+ insertion peaks were observed in the first cycle of the Edep IO sample as shown in Fig. 3(b) at ~ 3.36, 3.14, 2.22 and 1.85 V along the cathodic scan, and are attributed to efficient lithiation of more accessible, but thinner V_2O_5 material. Subsequent delithiation on the anodic scan occurs at ~3.52 V for the Edep electrode, but at a much lower voltage (~2.57 V) for the Edep IO material. The thinner regions or accessible IO V_2O_5 permit specific phase changes during the initial voltammetric polarization [51], evidenced by the multiple cathodic peaks associated with intercalation, and reduced overpotential for reversible de-intercalation for the IO cathode material.

The subsequent cycles for both samples are much smoother than the initial cycles due to the formation of an irreversible ω-$Li_\chi V_2O_5$ phase when cycled below 1.9 V. [47] For the Edep cathode, the potential difference between insertion and removal increases with cycling, but remains essentially constant for the Edep IO cathode (~ 2.22 V). The Li^+ removal peak for the Edep IO sample increased slightly from ~ 2.55 V during the 2nd cycle to ~2.63 V during the 10th cycle, showing a significantly reduced charging (oxidation) overpotential and a more stable energy density.

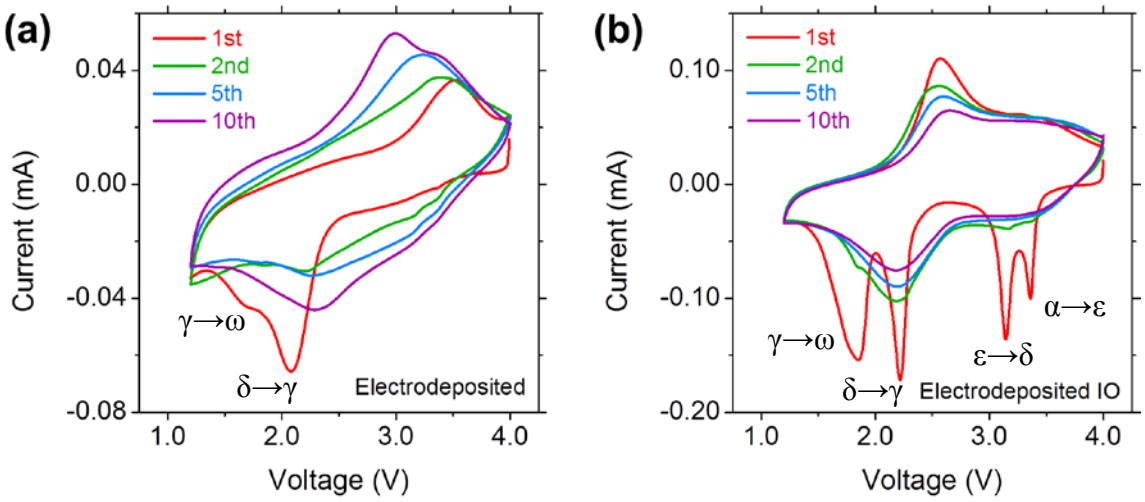

Fig. 3 Cyclic voltammograms for (a) electrodeposited material and (b) electrodeposited IO, acquired at a scan rate of 0.1 mV s^{-1}.

To determine the structural and mechanical stability of via changes to the IO atomic and/or molecular structure during discharging, linear sweep voltammograms were conducted from 4 V to the each of the reduction peak voltages (V_p) observed in the initial cyclic voltammograms, and examined *ex-situ* via Raman scattering spectroscopy (Fig. 4). The Raman spectra for the pristine Edep IO, matches that of orthorhombic V_2O_5 with a space group P*mmn* and D_{2h} point symmetry with the characteristic Raman modes at 102, 145, 196, 285, 304, 404, 482, 526, 701, and 994 cm^{-1}. [34] On lithium insertion, one of the first noticeable changes in the Raman signature for the sample removed at 3.36 V, is the change in the characteristic bending vibration at 145 cm^{-1} from the layered structure of the V_2O_5 (Fig. 4(a)).

This mode intensity reduces indicating a decrease in structural order between van der Waals separated lamellar vanadia sheets comprising the V_2O_5 structure. As the IO benefits from having these layers perpendicular to the current collector, this disorder constitutes a swelling into the available IO pore volume without detachment from the substrates as occurs with lamellar thin films. A slight shift towards a lower wavenumber of 143 cm^{-1} is also seen contrary to other reports on lithium insertion effects in bulk V_2O_5 [52-53] from galvanostatic discharge. However, an intensity increase in this V-O-V mode is observed when discharged to lower voltages or higher lithium mole fractions, and thus the IO (unlike thin films) maintains a lithiated layered V_2O_5 phase. Low wavenumber vibrations are observed at 96, 123, and 169 cm^{-1}, the disappearance of the 196 cm^{-1} mode and the progressive loss in intensity for these low wavenumber modes indicates an increase in local disorder within the layered structure (layer to layer order reduction). The formation of ε-phase $Li\chi V_2O_5$ has previously been reported with movement of the 483, 526 and 404 cm^{-1} Raman modes towards higher wavenumbers, associated with oxygen displacement along the *a*-axis of the unit cell.[53-54] The IO discharged 3.359 V likely represents an intermediate phase, moving towards the transition to the ε-phase.

The Raman signature for the sample discharged to 3.142 V shows the formation of a new peak at 957 cm^{-1} corresponding to and a further reduction in the V=O stretching mode frequency (lengthening of the vanadyl bond) to 978 cm^{-1}, as detailed in Fig. 4(b). The behavior described here for the Raman characteristics of IO V_2O_5 intercalated with increasing lithium uptake are mainly associated with the ε-phase of $Li_xV_2O_5$ as has been reported for crystalline thin films elsewhere.[52-54] The data confirms efficient lithium insertion into the crystalline V_2O_5 IO walls.

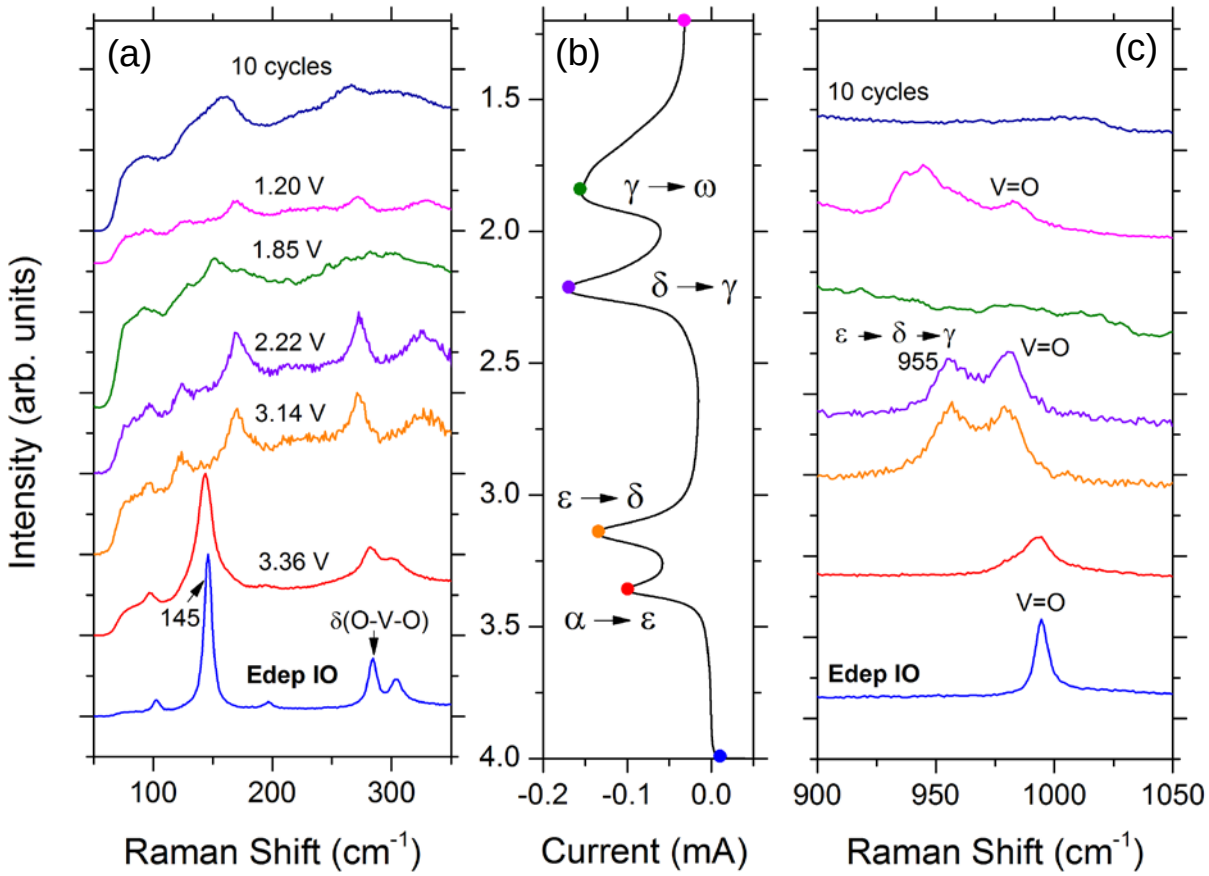

Fig. 4 (a,c) Raman scattering spectra from the as-prepared Edep V_2O_5 IO structure, and from IO electrodes after voltammetric scans (b) at a rate of 0.1 mV s^{-1}, to 3.359, 3.142, 2.217, 1.851 and 1.2 V. The spectrum acquired after 10 CV scans and after 10 cycles from 4.0 to 1.2 V is also shown.

The reduction in local order in the layered structure of the V_2O_5 IO walls is further corroborated by XRD, shown in Fig. 5. The XRD pattern observed for the Edep IO structure corresponds to orthorhombic V_2O_5, with a P*mnm* space grouping, with the (001) peak at $2\theta \sim 20.37°$. This (001) resonant peak shifts to lower angles and broadens as the discharge voltage decreases, which is indicative of lattice breathing within the solid material regions of the lamellar structure as a consequence of Li^+ intercalation.[55-57] An increase in the Li mole fraction of causes a puckering of the layers that affects V-O and V-O-V bonding and consequently a shift in the measured interplanar spacing of the (001) reflection. Since these layers in the IO structure are oriented perpendicular to the current collector, the widening does

not adversely affect electrical connection, and the electrolyte infiltrated pore volumes accommodate the swelling.

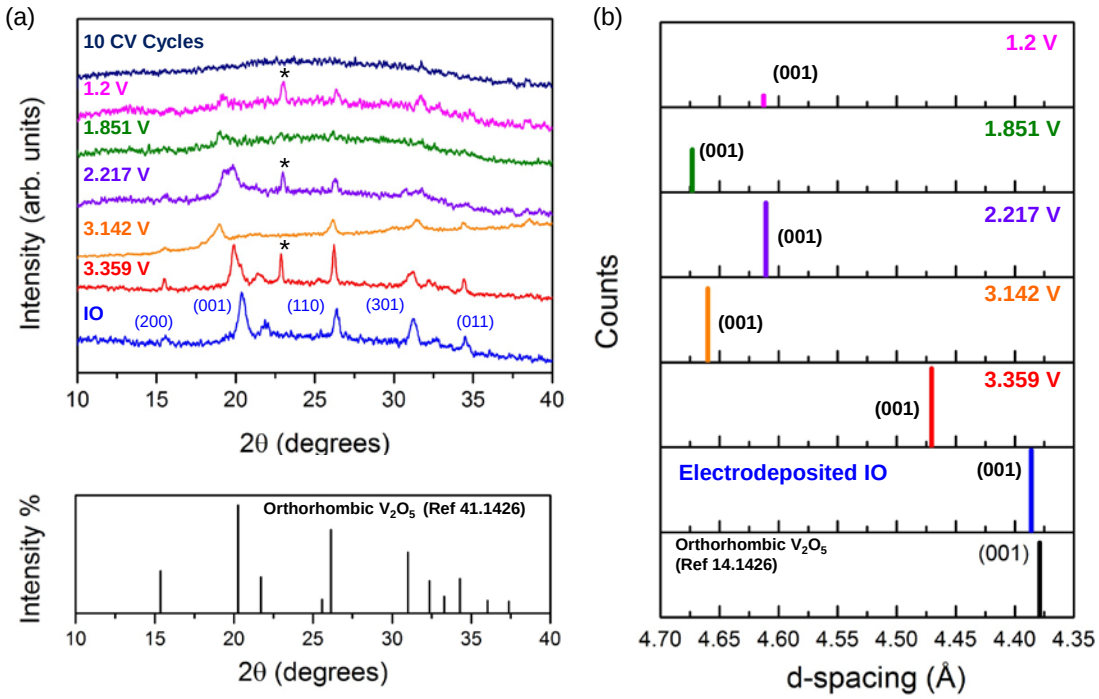

Fig. 5 (a) XRD patterns for the electrodeposited IO structure, before and after discharge at a rate of 0.1 mV s^{-1} to voltages corresponding to the reduction peaks seen in the cyclic voltammograms. The XRD after 10 discharge/charge cycles at a rate of 0.1 mV s^{-1} from 4.0-1.2 V is also overlaid. (b) Stick pattern corresponding to the interplanar spacing of the (001) reflection, illustrating its variation in position and intensity caused by lithiation of the IO.

The progression of the XRD spectra is directly correlated with the Raman spectra, showing gradual decrease in crystalline order as the material is discharged to 1.20 V, but importantly, the periodically porous IO structure is maintained – the crystallinity of the constituent walls varies. The d-spacing increases slightly between the discharge states at 3.142 V and 2.217 V and between 1.851 and 1.2 V, suggesting a recovery in layer structured or, as has been proposed in dedicated HRTEM analysis of *in-situ* electrochemical modifications to vanadium oxide, a lithiation-induced electrochemical 'welding' of regions caused by phase change inclusions (localized regions of different phase) throughout the structure. The variation in d-spacing below 3.142 V however, varies by just 0.006 nm. The initial charging cycle confirms that the 1st cycle capacity fade in an IO structure comprising

thin crystalline walls is not solely as a result of deleterious changes to the layered structure, and the consistency of the XRD response at 1.2 V to the observation of from Raman scattering data of strengthened V-O-V interlayer bonding confirms a mechanically stable IO structure. The XRD pattern for an Edep IO sample after 10 cycles shows an effectively amorphous structure.

It has previously been reported that many Li-ion battery electrode materials may store charge on the surface of the active material as well as through diffusion-based intercalation or alloying reactions. [58-60] Inverse opal structures offer increased surface area regions compared to other nanostructures, hence investigating charge storage on their surface is crucial to fully appreciate how IO structures store charge. This is, to our knowledge, the first report on the surface charge storage contributions to the total storage charge of an inverse opal structure. In order to examine the surface charge storage properties of Edep IO samples, the intercalation and capacitive contributions to the measured current were determined from analysis of CV curves obtained at various scan rates. The measured current, i, at a fixed potential, V can be described as the combination of capacitive effects ($k_1 v$) and diffusion controlled insertion ($k_2 v^{1/2}$) according to [61] $i(V,t) = k_1 v + k_2 v^{1/2}$, where v is the scan rate. By determining k_1 and k_2 it is possible to distinguish between the currents arising from Li^+ insertion and those occurring from capacitive processes. Cyclic voltammograms for an Edep IO sample were acquired for a series of scan rates ranging from 10 – 50 mV s^{-1}, as shown in Fig. 6(a). CVs were acquired at faster rates than the CVs presented in Fig. 3(b) as surface charge storage occurs faster than slower diffusion based charge storage. Consequently the discrete Li^+ insertion and removal peaks which were previously observed at slower scan rates are not as well defined at faster scan rates.

Capacitive charge storage may be due to double layer charging and pseudocapacitance and it can be characterized by analyzing CV curves at various scan rates according to [62] $i(V,t) = av^b$, where the measured current i obeys a power law relationship with the scan rate

v. Both *a* and *b* are adjustable parameters, *b*-exponent values are determined from the slope of the plot of log (*i*) vs log (*v*). There are two well defined conditions for *b*: $b = 0.5$ and $b = 1.0$. [63] When $b = 0.5$, the measured current is said to be primarily due to a faradaic process that may include intercalation, alloying etc. When $b = 1.0$, the measured current is representative of a capacitive response. The Li^+ insertion peaks for Edep IO samples, as determined from cyclic voltammetry, occur below 2.6 V. Hence, the *b*-values between 2.6 V and the lower potential limit of 1.2 V are shown in Fig. 6(b) and they are overlaid on the measured current of the first cathodic scan in the same potential range at a scan rate of 10 mV s^{-1}.

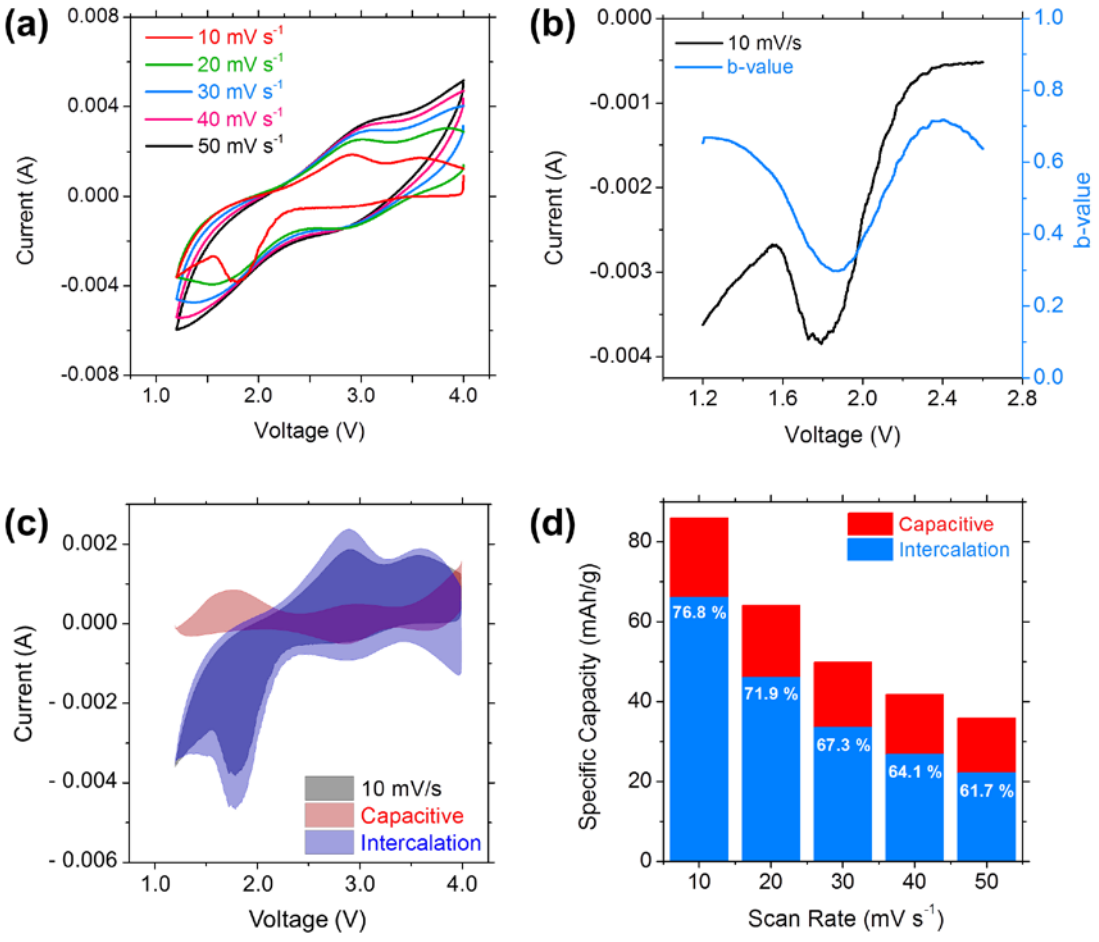

Fig. 6 (a) Cyclic voltammograms for Edep IO cycled at various scan rates, (b) Calculated *b*-values for Edep IO overlaid on the first cathodic scan at a scan rate of 10 mV/s, (c) Intercalation (blue) and capacitive (red) contributions to the total measured current (black) for Edep IO at a scan rate of 10 mV/s, (d) Intercalation (blue) and capacitive (red) contributions to specific capacity for Edep IO.

The *b*-values at 2.4 V were ~ 0.72, indicating that the measure current is likely due to a combination of intercalation and capacitive processes. The dominant Li^+ insertion peak for Edep IO at a scan rate of 10 mV s^{-1} occurs at ~ 1.79 V. The *b*-value at this this potential was ~ 0.32, indicating that the measured current at this potential is primarily due to intercalation processes.

The voltage profiles for the intercalation (blue area) and capacitive (red area) currents were compared with the total measured current (grey area) for Edep IO for scan rates in the range 10 - 50 mV/s, as shown in Fig. 6(c) and Fig. S3. The peaks in the blue curve, due to intercalation processes, are in close agreement with the peaks observed in the as measured current. This implies that the total charge stored is predominately due to intercalation based processes. The main Li^+ insertion peak occurred at ~ 1.79 V in the cathodic scan. The sum of the capacitive current at this potential (0.844 mA) and the intercalation current (- 4.680 mA), is in excellent agreement (-3.835 mA) with the measured current which had a value of -3.840 mA and verifies accurate deconvolution into the capacitive current curve and the intercalation current curve.

The intercalation and capacitive contributions towards the total cathodic specific capacity for Edep IO are shown in Fig. 6(d). The % of specific capacity due to intercalation processes decreased as the scan rate increased, from 78.6 % at 10 mV s^{-1} to 61.7 % at 50 mV s^{-1}. This shows that with increased cycling, less charge is stored due to Li^+ insertion. The consequence of this is a fading in specific capacity values, which was also observed in galvanostatic tests. The % of specific capacity due to capacitive processes is greater when the scan rate is faster, however the actual total capacity values decreased by ~31%. It is clear that the capacity fading in the capacitive contributions to the total specific capacity is not as severe as those from reversible intercalation contributions. This suggests that capacitive charge storage is not as destructive to the Edep IO structure as intercalation charge storage, and for

the latter, the IO structure helps to maintain capacity retention during cycling under potentiodynamic conditions.

Longer cycle life tests of Edep IO coin cell lithium batteries. An Edep IO sample was galvanostatically cycled 100 times in a potential window of 4.0 – 1.2 V using a C-rate of 0.2 C. The discharge and charge curves for the 2^{nd}, 50^{th} and 100^{th} cycles are shown in Fig. 7(a). The Li mole fraction in V_2O_5 decreased from ~1.03 mol after the 2^{nd} discharge to ~ 0.61 mol after the 50^{th} discharge and decreased further to ~ 0.35 mol after the 100^{th} discharge and is reflected in the specific capacity values over 100 cycles as shown in Fig. 7(b). The discharge capacity for the 2^{nd} cycle was ~151.52 mAh g^{-1}, this value decreased to ~50.86 mAh g^{-1} after the 100^{th} cycle, corresponding to a ~ 66% loss in the initial capacity. These capacity values are greater than values which have been previously reported for other V_2O_5 nanostructured cathode materials. [64-66] The walls of the IO structure, shown in Figs 7(c) and (d) appear thicker after 100 cycles due to volume changes associated with lithiation and some regions of the IO network appear pulverized, which may contribute to the capacity fading seen in Fig. 7(b). The whiteness in secondary electron emission from e-beam charging during imaging indicates either a reduction in electric conductivity of the lithiated species or contributions from dried electrolyte salt. However, the IO cell's capacity fading is linked to the change in the degree of lithiation of the IO material – the reduction in specific capacity scales with the reduction in the Li mole fraction (and availability of Li over long cycling periods in the electrolyte)). For the IO, material breakup, changes in electronic conductivity etc. are not as deleterious as is found in bulk materials – the interconnectivity of the IO material maintains stable coulometric efficiency.

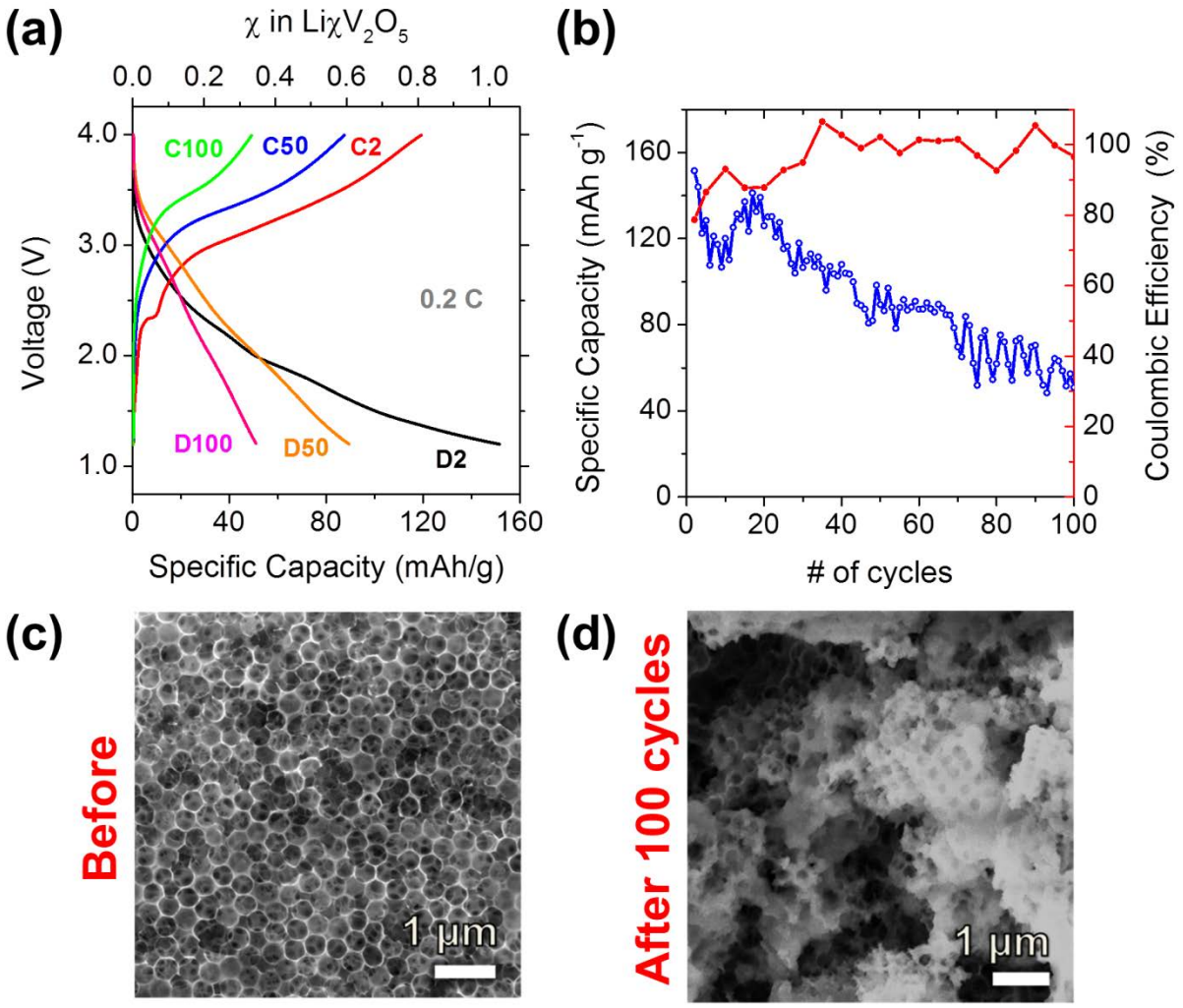

Fig. 7 (a) 2nd, 50th and 100th discharge and charge curves for Edep IO material, cycled at a C-rate of 0.2 C (b) Specific capacities and coulombic efficiencies for Edep IO over 100 cycles, SEM images of Edep IO material (c) before and (d) after 100 cycles.

The electrochemical performance of V_2O_5 Edep IO cathodes were also evaluated in a 3-electrode flooded cell to examine two important aspects: (1) to assess the influence of excess electrolyte on cycle stability and capacity fade by ensuring full lithiation upon discharge in the IO with reference to a chemically stable, unmodified Li reference, and (2) to assess the suitability of transparent conducting oxide (TCO) current collectors for single-side transparent thin film lithium batteries.

Firstly Edep IO samples on stainless steel were evaluated in a 3-electrode flooded cell. The specific capacity values obtained for an Edep IO sample on stainless steel foil tested in a

3-electrode flooded cell correlate well with those obtained in the 2-electrode coin cell as shown in Fig. S4. The specific capacity in the 3-electrode flooded cell decreased from ~ 176.07 mAh g^{-1}, after the 2^{nd} discharge, maintaining ~ 82.86 mAh g^{-1} after the 100^{th} discharge. This corresponds to an increased capacity retention (~47% retention of the initial capacity) for tests performed in a flooded cell. This data suggests that an excess of electrolyte is beneficial to electrochemical performance of highly porous materials, even though that are porous on the macro-scale. The dedicated comparison of flooded vs coin cell measurements of IO cathodes in thin film lithium batteries confirms that active material wetting by the electrolyte is important especially for structures that are already limited in terms of gravimetric energy density, assuming no dry-out of a limited quantity of separator-soaked electrolyte occurs.

An SEM image of an Edep IO sample prepared on an FTO substrate is shown in Fig. 8(a). The IO morphology grown on FTO substrates is quite similar to the Edep IO prepared on stainless steel (Fig. 8(a)). The voltage profiles for the 2^{nd}, 50^{th} and 75^{th} cycles for an Edep sample on an FTO current collector are shown in Fig. 8(b). For comparison, in the 2-electrode split cell ~ 0.35 mol of Li was inserted per mole of V_2O_5, after the 75^{th} cycle, whereas ~ 1.30 mol of Li was inserted into the Edep sample on the FTO current collector. The Edep IO on FTO demonstrated excellent capacity retention (negligible capacity loss after the 2^{nd} cycle, with just ~15% loss from 1^{st} to 2^{nd} cycle) over 75 cycles, with limited capacity fading in the first few cycles and a 75^{th} cycle capacity of ~191 mAh g^{-1}. This is a significant improvement over Edep IO on stainless steel in coin cells, which suffered more severe capacity fading issues. The calculated energy density for Edep V_2O_5 IO on FTO coated glass is ~ 587.80 Wh kg^{-1}, this is lower than the theoretical energy density for $Li_{\chi}CoO_2$ (~1100 Wh kg^{-1}) but comparable to experimental values (250 Wh kg^{-1}). [67]

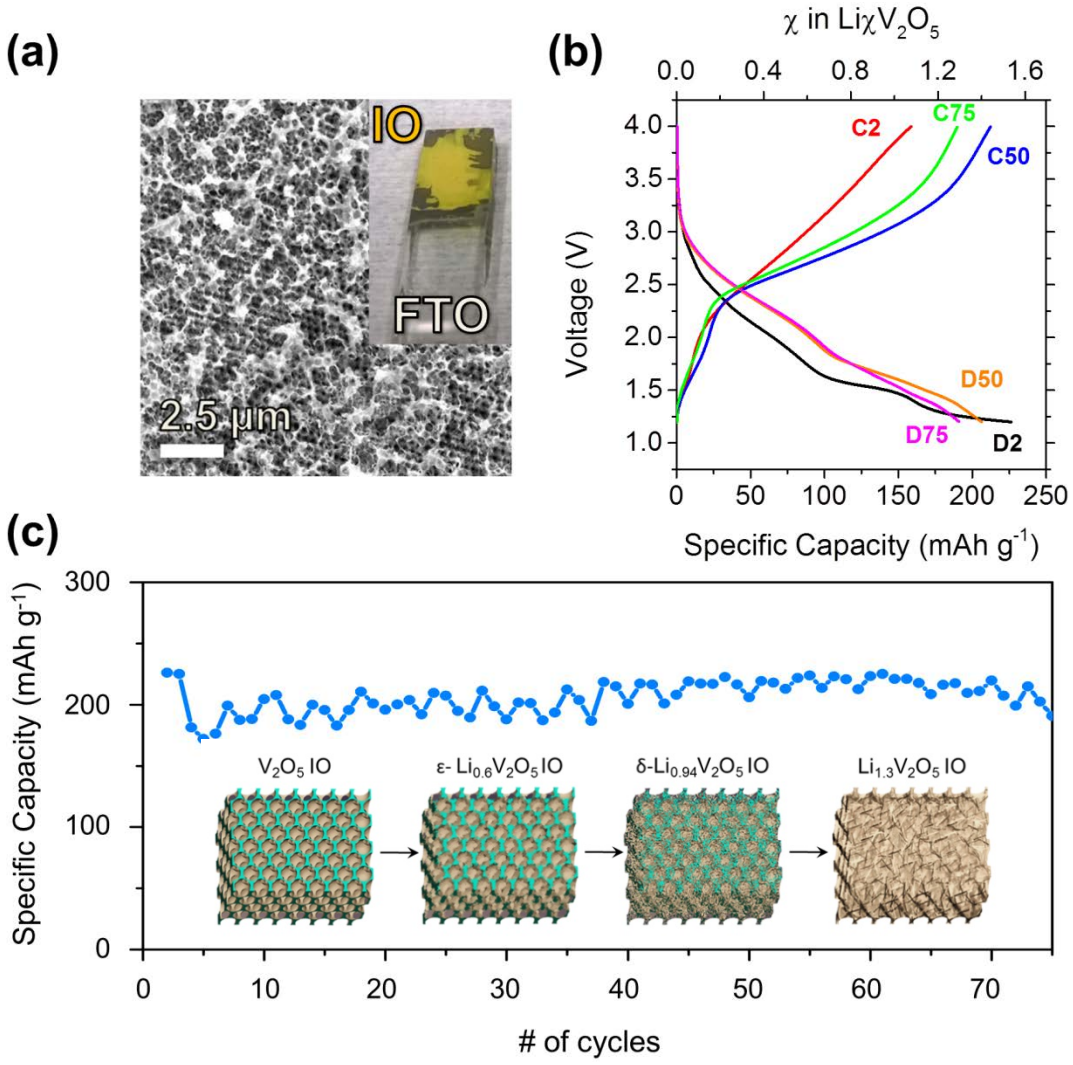

Fig. 8 (a) SEM and optical images of Edep IO structure prepared on FTO-coated glass, (b) 2nd, 50th and 75th discharge and charge curves for Edep IO material on FTO-coated glass, cycled at a C-rate of 0.4 C. (c) Specific capacity as a function of cycle number for Edep IO on FTO-coated glass. The schematic indicates the phase changes that occur during discharge, and the final cycled phase of the Edep IO lithium battery that maintains interconnectivity of material on a TCO.

An electrochemical assessment of the FTO-coated glass substrate by itself indicates that an almost negligible amount of lithium alloying with Sn [68] present in the FTO-coated glass substrate, as shown in Fig. S5. The first discharge for a blank FTO sample discharged at 30 µA took only ~ 300 s whereas the first discharge for an Edep IO sample prepared on FTO took > 52,000 s. This suggests that there is a negligible contribution from the FTO-coated glass current collector. To further investigate this we performed cyclic voltammetry of a blank

FTO coated glass sample and an Edep IO sample prepared on FTO coated glass, a comparison of the first cycle acquired at a scan rate of 0.1 mV/s is presented in Fig. S6. The current measured during the first cycle also suggests that there is a negligible contribution from the FTO-coated glass current collector.

Excessive cycling of a material on FTO results in discolouration of the transparent current collector, with minor change to transparency noted after 10 cycles (Fig. S7), although the electrode remains remarkably stable. Morphologically, little difference is found between the FTO-coated glass before and after 10 cycles (Fig. S7 (f) and (g)). The stainless steel substrates used in this study were quite thin (~0.5 mm), during the preparation of the Edep IO material, the substrates were heated to 300 ^{o}C, which can cause the steel to expand and then contract upon cooling. This expansion and contraction may cause cracks in the IO structure and a delamination of material from the current collector. In contrast to this the FTO coated glass used in this study was quick thick (~ 3 mm), consequently after heating and cooling the IO structure maintains rigidity and electrical contact with the FTO current collector than the stainless steel current collector, such that the semitransparent cathode retained capacity of 75 cycles with almost no loss. The specific capacity values obtained for V_2O_5 IO samples on FTO coated glass are greater than capacity values reported for several vanadium oxide nanostructures including nanourchins [69], nanobelts [70] and nanosheets [71]. Structured porous electrodes that rearrange Li-accessible insertion regions to an excess electrolyte that ensures maximum lithiation during discharging, can greatly improve the capacity retention and high cycle life electrode stability, much higher *specific* capacity (even for a porous material) and round-trip cycle efficiency in thin film lithium batteries.

Conclusions

From initial galvanostatic discharge-charge profiling, we demonstrated that both Edep and Edep IO thin film lithium battery materials offer increased capacity retention compared to bulk V_2O_5 and excellent rate capability. Cyclic voltammetry indicated that even though Edep and Edep IO V_2O_5 materials are both orthorhombic V_2O_5, Li^+ was inserted at different potentials, and correlated to the structure of the IO whereby the open vdW gaps in layered V_2O_5 are accessible to the electrolyte in the IO structure. Raman scattering and XRD characterization was performed to help determine the structural and phase alterations on lithium insertion and to what level structural degradation occurs. This process highlighted the stress incurred by the interlayer widening and formation of the ε-LiχV_2O_5 phase.

Cyclic voltammetry also uncovered the relative contributions of intercalation and capacitive processes towards the measured current and it was determined that a portion of charge is stored at the surface the IO structure. However, the total charge stored is predominately due to intercalation processes. IO thin film lithium batteries on stainless steel demonstrated significant initial capacity values of ~151.52 mAh g^{-1}, but significant fading occurred during 100 cycles to ~50.86 mAh g^{-1} due to structural and resistance changes within the IO material. Edep IO prepared on a transparent current collector (FTO) and tested in a 3-electrode flooded cell demonstrated significantly improved capacity retention compared to stainless steel-contacted electrodes in coin cells. The increased performance is likely a combination of factors: increased wetting of the IO electrode due to the excess of electrolyte and better adhesion between the IO structure and the FTO substrate. When cycled on FTO, Edep IO thin film batteries demonstrated high initial capacities and outstanding capacity retention. The discharge capacity after 75 cycles (~190.88 mAh g^{-1}) was higher than the typical initial capacity (140 mAh g^{-1}) for $LiCoO_2$, the most commonly used cathode material in commercial Li-ion batteries and several other vanadium oxide nanostructures. Hence

electrodeposited V_2O_5 IO samples are a promising candidate for use as a cathode material for future advanced Li-ion batteries.

Associated Content

Supporting Information

Comparative first discharge curves for bulk V_2O_5, electrodeposited material and electrodeposited inverse opal, analysis of intercalation and capacitive contributions to the total measured current for Edep IO from cyclic voltammetric measurements at a range of scan rates, specific capacity as a function of cycle number for V_2O_5 Edep IO on stainless steel in a 2-electrode split cell and 3-electrode flooded cell, and discharge-charge curves for (a) blank FTO-coated glass and electrodeposited V_2O_5 IO on FTO-coated glass. The Supporting Information is available free of charge on the ACS Publications website at DOI: XXX.

Author Information

Corresponding Author. *Email: c.odwyer@ucc.ie; Tel: +353 (0)21 4902732; Fax: +353 (0)21 4274097

Notes: The authors declare no competing financial interest.

Acknowledgements

Eileen Armstrong acknowledges the support of the Irish Research Council under award RS/2010/2920. We acknowledge support from the Irish Research Council's New Foundations Award. Support from Science Foundation Ireland under grant no. 07/BK/1232a-STTF11 is also acknowledged. This research has received funding from the Seventh Framework

Programme FP7/2007-2013 (Project STABLE) under grant agreement no. 314508. This work was also supported by SFI under the National Access Programme (NAP 417), and through an SFI Technology Innovation and Development Award under contract no. 13/TIDA/E2761. This publication has also emanated from research supported in part by a research grant from SFI under Grant Number 14/IA/2581.

References

1. Zhu, J.; Cao, L.; Wu, Y.; Gong, Y.; Liu, Z.; Hoster, H. E.; Zhang, Y.; Zhang, S.; Yang, S.; Yan, Q.; Ajayan, P. M.; Vajtai, R., Building 3D Structures of Vanadium Pentoxide Nanosheets and Application as Electrodes in Supercapacitors. *Nano Lett.* **2013,** *13*, 5408-5413.
2. Scrosati, B.; Garche, J., Lithium Batteries: Status, Prospects and Future. *J. Power Sources* **2010,** *195*, 2419-2430.
3. Roberts, M.; Johns, P.; Owen, J.; Brandell, D.; Edstrom, K.; El Enany, G.; Guery, C.; Golodnitsky, D.; Lacey, M.; Lecoeur, C.; Mazor, H.; Peled, E.; Perre, E.; Shaijumon, M. M.; Simon, P.; Taberna, P.-L., 3D Lithium ion Batteries-from Fundamentals to Fabrication. *J. Mater. Chem.* **2011,** *21*, 9876-9890.
4. Rolison, D. R.; Long, J. W.; Lytle, J. C.; Fischer, A. E.; Rhodes, C. P.; McEvoy, T. M.; Bourg, M. E.; Lubers, A. M., Multifunctional 3D Nanoarchitectures for Energy Storage and Conversion. *Chem. Soc. Rev.* **2009,** *38*, 226-252.
5. Van Gough, D.; Juhl, A. T.; Braun, P. V., Programming Structure into 3D Nanomaterials. *Mater. Today* **2009,** *12*, 28-35.
6. Ergang, N. S.; Lytle, J. C.; Lee, K. T.; Oh, S. M.; Smyrl, W. H.; Stein, A., Photonic Crystal Structures as a Basis for a Three-Dimensionally Interpenetrating Electrochemical-Cell System. *Adv. Mater.* **2006,** *18*, 1750-1753.
7. Ergang, N. S.; Fierke, M. A.; Wang, Z.; Smyrl, W. H.; Stein, A., Fabrication of a Fully Infiltrated Three-Dimensional Solid-State Interpenetrating Electrochemical Cell. *J. Electrochem. Soc.* **2007,** *154*, A1135-A1139.
8. Armstrong, E.; O'Dwyer, C., Artificial Opal Photonic Crystals and Inverse Opal Structures–Fundamentals and Applications from Optics to Energy Storage. *J. Mater. Chem. C* **2015**.
9. Bhatt, M. D.; O'Dwyer, C., Recent Progress in Theoretical and Computational Investigations of Li-ion Battery Materials and Electrolytes. *Phys. Chem. Chem. Phys.* **2015,** *17*, 4799-4844.
10. Sakamoto, J. S.; Dunn, B., Hierarchical Battery Electrodes Based on Inverted Opal Structures. *J. Mater. Chem.* **2002,** *12*, 2859-2861.
11. Lytle, J. C., Inverse Opal Nanoarchitectures as Lithium-Ion Battery Materials. In *Nanotechnology for Lithium-Ion Batteries*, Abu-Lebdeh, Y.; Davidson, I., Eds. Springer US: **2013**; Chapter 2, pp 13-41.
12. Kang, D.-Y.; Kim, S.-O.; Chae, Y. J.; Lee, J. K.; Moon, J. H., Particulate Inverse Opal Carbon Electrodes for Lithium-Ion Batteries. *Langmuir* **2013,** *29*, 1192-1198.

13. Li, X.; Dhanabalan, A.; Gu, L.; Wang, C., Three-Dimensional Porous Core-Shell Sn@Carbon Composite Anodes for High-Performance Lithium-Ion Battery Applications. *Adv. Energy Mater.* **2012,** *2*, 238-244.
14. Zhou, W.; Lin, L.; Wang, W.; Zhang, L.; Wu, Q.; Li, J.; Guo, L., Hierarchial Mesoporous Hematite with "Electron-Transport Channels" and Its Improved Performances in Photocatalysis and Lithium Ion Batteries. *J. Phys. Chem. C* **2011,** *115*, 7126-7133.
15. Doherty, C. M.; Caruso, R. A.; Smarsly, B. M.; Drummond, C. J., Colloidal Crystal Templating to Produce Hierarchically Porous $LiFePO_4$ Electrode Materials for High Power Lithium Ion Batteries. *Chem. Mater.* **2009,** *21*, 2895-2903.
16. Zhang, H.; Braun, P. V., Three-Dimensional Metal Scaffold Supported Bicontinuous Silicon Battery Anodes. *Nano Lett.* **2012,** *12*, 2778-2783.
17. Zhang, H.; Yu, X.; Braun, P. V., Three-dimensional Bicontinuous Ultrafast-Charge and -Discharge Bulk Battery Electrodes. *Nat. Nanotechnol.* **2011,** *6*, 277-281.
18. Osiak, M.; Geaney, H.; Armstrong, E.; O'Dwyer, C., Structuring Materials for Lithium-ion Batteries: Advancements in Nanomaterial Structure, Composition, and Defined Assembly on Cell Performance. *J. Mater. Chem. A* **2014,** *2* 9433-9460.
19. Ding, Y.-L.; Wen, Y.; Wu, C.; van Aken, P. A.; Maier, J.; Yu, Y., 3D V_6O_{13} Nanotextiles Assembled from Interconnected Nanogrooves as Cathode Materials for High-Energy Lithium Ion Batteries. *Nano Lett.* **2015,** *15*, 1388-1394.
20. McNulty, D.; Buckley, D. N.; O'Dwyer, C., Synthesis and Electrochemical Properties of Vanadium Oxide Materials and Structures as Li-ion Battery Positive Electrodes. *J. Power Sources* **2014,** *267*, 831-873.
21. McNulty, D.; Buckley, D. N.; O'Dwyer, C., Polycrystalline Vanadium Oxide Nanorods: Growth, Structure and Improved Electrochemical Response as a Li-Ion Battery Cathode Material. *J. Electrochem. Soc.* **2014,** *161*, A1321-A1329.
22. Wei, Q.; Tan, S.; Liu, X.; Yan, M.; Wang, F.; Li, Q.; An, Q.; Sun, R.; Zhao, K.; Wu, H.; Mai, L., Novel Polygonal Vanadium Oxide Nanoscrolls as Stable Cathode for Lithium Storage. *Adv. Funct. Mater.* **2015,** *25*, 1773-1779.
23. Liu, J.; Wang, X.; Peng, Q.; Li, Y., Vanadium Pentoxide Nanobelts: Highly Selective and Stable Ethanol Sensor Materials. *Adv. Mater.* **2005,** *17*, 764-767.
24. Yang, Y.; Kim, D.; Yang, M.; Schmuki, P., Vertically aligned mixed V_2O_5-TiO_2 nanotube arrays for supercapacitor applications. *Chem. Commun.* **2011,** *47*, 7746-7748.
25. Rui, X.; Lu, Z.; Yu, H.; Yang, D.; Hng, H. H.; Lim, T. M.; Yan, Q., Ultrathin V_2O_5 nanosheet cathodes: realizing ultrafast reversible lithium storage. *Nanoscale* **2013,** *5*, 556-560.
26. Qu, Q.; Zhu, Y.; Gao, X.; Wu, Y., Core–Shell Structure of Polypyrrole Grown on V_2O_5 Nanoribbon as High Performance Anode Material for Supercapacitors. *Adv. Energy Mater.* **2012,** *2*, 950-955.
27. Zhou, S.; Yang, X.; Lin, Y.; Xie, J.; Wang, D., A Nanonet-Enabled Li Ion Battery Cathode Material with High Power Rate, High Capacity, and Long Cycle Lifetime. *ACS Nano* **2012,** *6*, 919-924.
28. Zhai, T.; Liu, H.; Li, H.; Fang, X.; Liao, M.; Li, L.; Zhou, H.; Koide, Y.; Bando, Y.; Golberg, D., Centimeter‐Long V_2O_5 Nanowires: From Synthesis to Field‐Emission, Electrochemical, Electrical Transport, and Photoconductive Properties. *Adv. Mater.* **2010,** *22*, 2547-2552.
29. Li, Y.; Yao, J.; Uchaker, E.; Yang, J.; Huang, Y.; Zhang, M.; Cao, G., Leaf‐Like V_2O_5 Nanosheets Fabricated by a Facile Green Approach as High Energy Cathode Material for Lithium‐Ion Batteries. *Adv. Energy Mater.* **2013,** *3*, 1171-1175.
30. O'Dwyer, C.; Navas, D.; Lavayen, V.; Benavente, E.; Ana, M. A. S.; González, G.; Newcomb, S. B.; Torres, C. M. S., NanoUrchin: The Formation and Structure of High

Density Spherical Clusters of Vanadium Oxide Nanotubes. *Chem. Mater.* **2006,** *18*, 3016-3022.
31. Yu, D. M.; Chen, C. G.; Xie, S. H.; Liu, Y. Y.; Park, K.; Zhou, X. Y.; Zhang, Q. F.; Li, J. Y.; Cao, G. Z., Mesoporous Vanadium Pentoxide Nanofibers with Significantly Enhanced Li-ion Storage Properties by Electrospinning. *Energy Environ. Sci.* **2011,** *4*, 858–861.
32. An, Q.; Wei, Q.; Zhang, P.; Sheng, J.; Hercule, K. M.; Lv, F.; Wang, Q.; Wei, X.; Mai, L., Three‐Dimensional Interconnected Vanadium Pentoxide Nanonetwork Cathode for High‐Rate Long‐Life Lithium Batteries. *Small* **2015,** *11*, 2654‐2660.
33. Armstrong, E.; O'Connell, J.; Holmes, J. D.; O'Dwyer, C., 3D Vanadium Oxide Inverse Opal Growth by Electrodeposition. *J. Electrochem. Soc.* **2015,** *162*, D605-D612.
34. Armstrong, E.; Osiak, M.; Geaney, H.; Glynn, C.; O'Dwyer, C., 2D and 3D Vanadium Oxide Inverse Opals and Hollow Sphere Arrays. *CrystEngComm* **2014,** *16*, 10804-10815.
35. Vu, A.; Qian, Y.; Stein, A., Porous Electrode Materials for Lithium-Ion Batteries – How to Prepare Them and What Makes Them Special. *Adv. Energy Mater.* **2012,** *2*, 1056-1085.
36. Goodenough, J. B.; Kim, Y., Challenges for Rechargeable Li Batteries. *Chem. Mater.* **2009,** *22*, 587-603.
37. Stein, A., Energy storage: Batteries Take Charge. *Nat. Nanotechnol.* **2011,** *6*, 262-263.
38. Joannopoulos, J. D.; Villeneuve, P. R.; Fan, S., Photonic Crystals: Putting a New Twist on Light. *Nature* **1997,** *386*, 143-149.
39. Hachisu, S.; Yoshimura, S., Optical Demonstration of Crystalline Superstructures in Binary Mixtures of Latex Globules. *Nature* **1980,** *283*, 188-189.
40. Sanders, J. V., Colour of Precious Opal. *Nature* **1964,** *204*, 1151-1153.
41. Zi, J.; Yu, X.; Li, Y.; Hu, X.; Xu, C.; Wang, X.; Liu, X.; Fu, R., Coloration Strategies in Peacock Feathers. *Proc. Natl. Acad. Sci. U. S. A.* **2003,** *100*, 12576-12578.
42. Li, L.; Steiner, U.; Mahajan, S., Improved Electrochromic Performance in Inverse Opal Vanadium Oxide Films. *J. Mater. Chem.* **2010,** *20*, 7131-7134.
43. Tong, Z.; Hao, J.; Zhang, K.; Zhao, J.; Su, B.-L.; Li, Y., Improved Electrochromic Performance and Lithium Diffusion Coefficient in Three-dimensionally Ordered Macroporous V_2O_5 Films. *J. Mater. Chem. C* **2014,** *2*, 3651-3658.
44. Wang, Y.; Cao, G., Synthesis and Enhanced Intercalation Properties of Nanostructured Vanadium Oxides. *Chem. Mater.* **2006,** *18*, 2787-2804.
45. Livage, J., Optical and Electrical Properties of Vanadium Oxides Synthesized from Alkoxides. *Coord. Chem. Rev.* **1999,** *190–192*, 391-403.
46. Whittingham, M. S., The Role of Ternary Phases in Cathode Reactions. *J. Electrochem. Soc.* **1976,** *123*, 315-320.
47. Delmas, C.; Brèthes, S.; Ménétrier, M., ω-LixV_2O_5 — A New Electrode Material for Rechargeable Lithium Batteries. *J. Power Sources* **1991,** *34*, 113-118.
48. West, K.; Zachau-Christiansen, B.; Jacobsen, T.; Skaarup, S., Vanadium Oxide Xerogels as Electrodes for Lithium Batteries. *Electrochim. Acta* **1993,** *38*, 1215-1220.
49. Wang, S.; Li, S.; Sun, Y.; Feng, X.; Chen, C., Three-dimensional Porous V_2O_5 Cathode with Ultra High Rate Capability. *Energy & Environ. Sci.* **2011,** *4*, 2854-2857.
50. Mai, L.; An, Q.; Wei, Q.; Fei, J.; Zhang, P.; Xu, X.; Zhao, Y.; Yan, M.; Wen, W.; Xu, L., Nanoflakes‐Assembled Three‐Dimensional Hollow‐Porous V_2O_5 as Lithium Storage Cathodes with High‐Rate Capacity. *Small* **2014,** *10*, 3032-3037.
51. Chan, C. K.; Peng, H.; Twesten, R. D.; Jarausch, K.; Zhang, X. F.; Cui, Y., Fast, Completely Reversible Li Insertion in Vanadium Pentoxide Nanoribbons. *Nano Lett.* **2007,** *7*, 490-495.

52. Baddour-Hadjean, R.; Golabkan, V.; Pereira-Ramos, J. P.; Mantoux, A.; Lincot, D., A Raman Study of the Lithium Insertion Process in Vanadium Pentoxide Thin Films Deposited by Atomic Layer Deposition. *J. Raman Spectrosc.* **2002,** *33*, 631-638.
53. Baddour-Hadjean, R.; Pereira-Ramos, J. P.; Navone, C.; Smirnov, M., Raman Microspectrometry Study of Electrochemical Lithium Intercalation into Sputtered Crystalline V_2O_5 Thin Films. *Chem. Mater.* **2008,** *20*, 1916-1923.
54. Baddour-Hadjean, R.; Navone, C.; Pereira-Ramos, J. P., In situ Raman Microspectrometry Investigation of Electrochemical Lithium Intercalation into Sputtered Crystalline V_2O_5 Thin Films. *Electrochim. Acta* **2009,** *54*, 6674-6679.
55. O'Dwyer, C.; Gannon, G.; McNulty, D.; Buckley, D. N.; Thompson, D., Accommodating Curvature in a Highly Ordered Functionalized Metal Oxide Nanofiber: Synthesis, Characterization, and Multiscale Modeling of Layered Nanosheets. *Chem. Mater.* **2012,** *24*, 3981-3992.
56. Gannon, G.; O'Dwyer, C.; Larsson, J. A.; Thompson, D., Interdigitating Organic Bilayers Direct the Short Interlayer Spacing in Hybrid Organic–Inorganic Layered Vanadium Oxide Nanostructures. *J. Phys. Chem. B* **2011,** *115*, 14518-14525.
57. O'Dwyer, C.; Lavayen, V.; Tanner, D. A.; Newcomb, S. B.; Benavente, E.; González, G.; Torres, C. M. S., Reduced Surfactant Uptake in Three Dimensional Assemblies of VO_x Nanotubes Improves Reversible Li^+ Intercalation and Charge Capacity. *Adv. Funct. Mater.* **2009,** *19*, 1736-1745.
58. Winny, D.; Jeffrey, S. S.; Bruce, D., Electrochemical Properties of Vanadium Oxide Aerogels. *Sci. Tech. Adv. Mater.* **2003,** *4*, 3.
59. Simon, P.; Gogotsi, Y.; Dunn, B., Where Do Batteries End and Supercapacitors Begin? *Science* **2014,** *343*, 1210-1211.
60. Augustyn, V.; Come, J.; Lowe, M. A.; Kim, J. W.; Taberna, P.-L.; Tolbert, S. H.; Abruña, H. D.; Simon, P.; Dunn, B., High-rate Electrochemical Energy Storage through Li^+ Intercalation Pseudocapacitance. *Nat. Mater.* **2013,** *12*, 518-522.
61. Huang, C.; Grant, P. S., One-step Spray Processing of High Power All-Solid-State Supercapacitors. *Sci. Rep.* **2013,** *3*, 2393.
62. Lindström, H.; Södergren, S.; Solbrand, A.; Rensmo, H.; Hjelm, J.; Hagfeldt, A.; Lindquist, S.-E., Li^+ Ion Insertion in TiO_2 (Anatase). 2. Voltammetry on Nanoporous Films. *J. Phys. Chem. B* **1997,** *101*, 7717-7722.
63. Brezesinski, T.; Wang, J.; Tolbert, S. H.; Dunn, B., Ordered Mesoporous α-MoO_3 with Iso-oriented Nanocrystalline Walls for Thin-film Pseudocapacitors. *Nat. Mater.* **2010,** *9*, 146-151.
64. Wang, H.-g.; Ma, D.-l.; Huang, Y.; Zhang, X.-b., Electrospun V_2O_5 Nanostructures with Controllable Morphology as High-Performance Cathode Materials for Lithium-Ion Batteries. *Chem. Eur. J.* **2012,** *18*, 8987-8993.
65. Li, H. X.; Jiao, L. F.; Yuan, H. T.; Zhang, M.; Guo, J.; Wang, L. Q.; Zhao, M.; Wang, Y. M., Factors Affecting the Electrochemical Performance of Vanadium Oxide Nanotube Cathode Materials. *Electrochem. Commun.* **2006,** *8*, 1693-1698.
66. Mohan, V. M.; Hu, B.; Qiu, W.; Chen, W., Synthesis, Structural, and Electrochemical Performance of V_2O_5 Nanotubes as Cathode Material for Lithium Battery. *J Appl Electrochem* **2009,** *39*, 2001-2006.
67. Whittingham, M. S., History, Evolution, and Future Status of Energy Storage. *Proceedings of the IEEE* **2012,** *100*, 1518-1534.
68. Osiak, M. J.; Armstrong, E.; Kennedy, T.; Sotomayor Torres, C. M.; Ryan, K. M.; O'Dwyer, C., Core–Shell Tin Oxide, Indium Oxide, and Indium Tin Oxide Nanoparticles on Silicon with Tunable Dispersion: Electrochemical and Structural Characteristics as a Hybrid Li-Ion Battery Anode. *ACS Appl. Mater. Interfaces* **2013,** *5*, 8195-8202.

69. Wang, J.; Cui, C.; Gao, G.; Zhou, X.; Wu, J.; Yang, H.; Li, Q.; Wu, G., A New Method to Prepare Vanadium Oxide Nano-urchins as a Cathode for Lithium ion Batteries. *RSC Adv.* **2015,** *5*, 47522-47528.
70. Qin, M.; Liang, Q.; Pan, A.; Liang, S.; Zhang, Q.; Tang, Y.; Tan, X., Template-free Synthesis of Vanadium Oxides Nanobelt Arrays as High-rate Cathode Materials for Lithium ion Batteries. *J.Power Sources* **2014,** *268*, 700-705.
71. Zeng, Y.; Gao, G.; Wu, G.; Yang, H., Nanosheet-structured Vanadium Pentoxide Thin Film as a Carbon- and Binder-free Cathode for Lithium-ion Battery Applications. *J Solid State Electrochem* **2015**, 1-10.